

Time-domain full-field optical coherence tomography (TD-FF-OCT) in ophthalmic imaging

Jinze Zhang^{*} , Viacheslav Mazlin^{*}, Keyi Fei, Albert Claude Boccara, Jin Yuan and Peng Xiao

Abstract: Ocular imaging plays an irreplaceable role in the evaluation of eye diseases. Developing cellular-resolution ophthalmic imaging technique for more accurate and effective diagnosis and pathogenesis analysis of ocular diseases is a hot topic in the cross-cutting areas of ophthalmology and imaging. Currently, ocular imaging with traditional optical coherence tomography (OCT) is limited in lateral resolution and thus can hardly resolve cellular structures. Conventional OCT technology obtains ultra-high resolution at the expense of a certain imaging range and cannot achieve full field of view imaging. In the early years, Time-domain full-field OCT (TD-FF-OCT) has been mainly used for *ex vivo* ophthalmic tissue studies, limited by the low speed and low full-well capacity of existing two-dimensional (2D) cameras. The recent improvements in system design opened new imaging possibilities for *in vivo* applications thanks to its distinctive optical properties of TD-FF-OCT such as a spatial resolution almost insensitive to aberrations, and the possibility to control the curvature of the optical slice. This review also attempts to look at the future directions of TD-FF-OCT evolution, for example, the potential transfer of the functional-imaging dynamic TD-FF-OCT from the *ex vivo* into *in vivo* use and its expected benefit in basic and clinical ophthalmic research. Through non-invasive, wide-field, and cellular-resolution imaging, TD-FF-OCT has great potential to be the next-generation imaging modality to improve our understanding of human eye physiology and pathology.

Keywords: cellular resolution, full-field OCT, ophthalmic imaging, optical coherence tomography

Received: 27 August 2022; revised manuscript accepted: 29 March 2023.

Background

After 30 years since its development, optical coherence tomography (OCT)^{1–4} continues to be increasingly applied to medical imaging, and especially in ophthalmology, because of its advantages of high-resolution and high-sensitivity imaging without contact with an eye. The most common OCT nowadays is spectral-domain OCT (SD-OCT).^{5–9} It relies on the spatially coherent source of low temporal coherence and spectrometer to obtain a one-dimensional (1D) axial in-depth reflectivity profile (the so-called A-line). By scanning the beam laterally, one can reconstruct two-dimensional (2D) cross-sectional images (B-scans) and three-dimensional (3D)

volumetric views.¹⁰ Historically, the cross-sectional images were the ones that opened the door for OCT clinical ophthalmology. By comprehensively and objectively observing and evaluating the parameters of the drusen within the retina, clinical doctors were empowered to diagnose and follow up on the offer activeness of treatment against wet age-related macular degeneration (wet AMD) – a challenging ocular condition.^{11–15}

Today modern clinical OCTs are very performant at reconstructing cross-sectional images – at scanning speed of 100 kHz and 1000 pixels field-of-view (FOV) 100 B-scans can be recorded in 1 s (0.01 s for a single B-scan), keeping the physiological

Ther Adv Chronic Dis

2023, Vol. 14: 1–19

DOI: 10.1177/
20406223231170146

© The Author(s), 2023.
Article reuse guidelines:
[sagepub.com/journals-
permissions](https://sagepub.com/journals-permissions)

Correspondence to:

Jin Yuan

State Key Laboratory of Ophthalmology, Zhongshan Ophthalmic Center, Sun Yat-sen University, Guangdong Provincial Key Laboratory of Ophthalmology and Visual Science, Jinsui Road 7, Guangzhou 510060, Guangdong, China.
yuanjincornea@126.com

Peng Xiao

State Key Laboratory of Ophthalmology, Zhongshan Ophthalmic Center, Sun Yat-sen University, Guangdong Provincial Key Laboratory of Ophthalmology and Visual Science, Jinsui Road 7, Guangzhou 510060, Guangdong, China.
xiaopengaddis@hotmail.com

Jinze Zhang

Keyi Fei

State Key Laboratory of Ophthalmology, Zhongshan Ophthalmic Center, Sun Yat-sen University, Guangdong Provincial Key Laboratory of Ophthalmology and Visual Science, Guangzhou, China

Viacheslav Mazlin

Albert Claude Boccara
ESPCI Paris, PSL University, CNRS, Langevin Institute, Paris, France

^{*}These authors contributed equally.



motions of the eye effectively frozen.¹⁶ However, cross-sectional imaging is not the most practical modality for evaluating all aspects of ocular health. For example, blood vessels of the retina and limbus of the eye are oriented primarily laterally, which makes en face views preferable as they directly show the vessel branching patterns and the propagating blood flow within them (angiography).¹⁷⁻¹⁹ Moreover, cells of the cornea and retina lie in the lateral sheets, therefore quantitative clinical diagnosis based on cell density requires face views. Unfortunately, SD-OCT is less adapted to en-face imaging compared with cross-sectional one. More precisely, to acquire an en face view, SD-OCT needs to scan not in one but in two directions, which requires considerable time (in fact the same time as for the acquisition of a 3D volume).²⁰⁻²² With the 100 kHz device a single 1000-pixel × 1000-pixel image is reconstructed in 10s – a too long time to avoid the destructive eye movement artifacts. The acquisition time can be reduced to suppress the movements, however, at a cost of considerably shrinking the visible FOV. Within small FOV, only a few cells can be visible, leading to low precision of potential quantitative diagnosis. The limited frame rate of en face acquisition also sets a low limit for the time precision of angiographic measurements.

Since the early days, in parallel to the spectral domain (Fourier domain) OCT, another class of en face OCT methods have been under development to increase en face imaging speed. Advances in camera technologies and light sources in recent years enabled the rise of en face OCT methods, such as Fourier-domain full-field OCT (FD-FF-OCT),²³⁻²⁶ also known as swept-source full-field OCT (SS-FF-OCT),²⁷⁻³⁰ line-field OCT (LF-OCT),³¹⁻³⁵ ultra-high-resolution OCT (UHR-OCT),³⁶⁻⁴² and so on. An excellent review of en face OCT methods can be found.⁴³ In this article, we will limit ourselves to a single method – time-domain full-field OCT (TD-FF-OCT) and its development progress and future in the ophthalmic imaging field.

Fundamentals of TD-FF-OCT

Basic principle

TD-FF-OCT, demonstrated by Beaulieu *et al.*, is an en face OCT that uses full-field illumination and a parallel array (camera) detection to

accelerate en face imaging.^{44,45} When the speed of axial or lateral motion is lower than the camera exposure time, TD-FF-OCT can capture all camera pixels without horizontal scanning, which leads to suppression of the potential motion artifacts coming from the sample. TD-FF-OCT's primary sectioning orientation is en face, there is usually no need to keep the large depth-of-field (DOF) optics. Its detection geometry makes it more suitable to maintain the best resolution at different depths by changing the focal plane according to the coherent plane. Therefore, typically high numerical aperture (NA) microscope objective can be used to achieve micrometer-level lateral resolution. The latter is given by the Rayleigh criterion extensively used in optical microscopy as shown in equation (1). Full-field illumination, 2D camera, and microscope objective largely remind of the classical microscope designs; however, TD-FF-OCT also adds the second optical arm with a reference mirror to achieve optical gating. Another essential requirement for optical gating is a light source of low temporal coherence, ensuring that light back-scattered from only one slice of the sample will interfere with the reflected light from the reference mirror. The more broadband is the light source spectrum – the smaller is the temporal coherence and the thinner is the interfering sample section [higher axial resolution; equation (2)]

$$\Delta x = \Delta y = \frac{0.61\lambda}{NA} \quad (1)$$

$$\Delta z = \frac{2 \ln 2}{\pi n} \cdot \frac{\lambda^2}{\Delta \lambda} \quad (2)$$

where Δx and Δy are the resolutions in lateral directions, Δz is the resolution in the axial direction measured by full-width-half maximum (FWHM), λ is the central wavelength and $\Delta \lambda$ is spectral bandwidth of the light source, and n is the refractive index of the sample tissue.⁴⁴ It can be noted from the above that the horizontal resolution is separated from the axial resolution, which is common in the OCT method (Figure 1). However, a high NA objective lens can limit the DOF of axial resolution.

Bright-field illumination in TD-FF-OCT can be achieved with low-cost light sources of low spatial coherence such as halogen lamps or light-emitting diodes (LED). These sources bring the

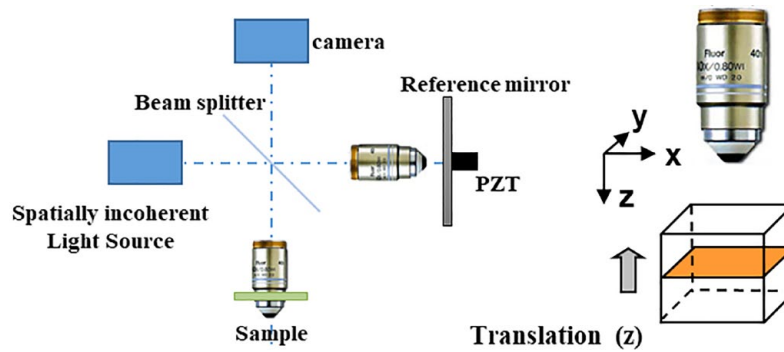


Figure 1. Schematic of FF-OCT. Left: Diagram of a conventional FF-OCT in a Linnik interferometer. Right: Diagram showing FF-OCT takes en face images with planes $\{xy\}$ that are perpendicular to the optical axis $\{z\}$. BS, beam splitter; PZT, piezoelectric transducer.

advantage that they produce images free from unwanted cross-talk effects (speckle)⁴⁶ that typically degrade the images in the coherent-light OCTs.

Image reconstruction

It is worth stating that the equations in this section are mainly used by TD-FF-OCT in human *in vivo* eye imaging, and may differ in detail for other uses of imaging, and the imaging equations in other scenarios and more details can be found in the references.^{44,47} TD-FF-OCT first prevents defocus light from reaching the detector, then detects the entire bright field, and then relies on the rear demodulation scheme to generate the optical part. Each bright-field image on the camera contains: (1) ballistic single-scattered light from the sample optical section and reflected light from the reference mirror that interferes ('coherent' light) and (2) light that does not participate in interference ('incoherent' light) from the other layers of the sample, from the reference mirror, stray light reflected from optical components, as well as the multiply-scattered light from the sample optical section. The goal of TD-FF-OCT is to suppress the 'incoherent' light and keep the 'coherent' light thus producing an optical section. This is done by using the fact that the optical phase of interfering light can be easily controlled by shifting the reference mirror. By varying the reference mirror position in time (thus the name 'time-domain' FF-OCT), one can record several bright-field images with different phases. Change in the phase corresponds to different intensities on the camera and different brightness of the

detected pixel. Using the fact that the phase modulation affects only the intensity of interfering light, one can easily reject the static 'incoherent' background in the images and retrieve an optical section. There exist many phase-modulation schemes that differ in the number of bright-field images used. In the simplest example of two-phase modulation, two images are acquired on the camera as given by Equation (3)^{48,49}

$$I_1(x, y) = \frac{I_0}{4} \cdot \left\{ \begin{array}{l} R_{inc} + R_{coh-sample} + R_{ref} + \\ 2\sqrt{R_{coh-sample} \cdot R_{ref}} \cdot \cos[\varphi(x, y) + \psi_1] \end{array} \right\}$$

$$I_2(x, y) = \frac{I_0}{4} \cdot \left\{ \begin{array}{l} R_{inc} + R_{coh-sample} + R_{ref} + \\ 2\sqrt{R_{coh-sample} \cdot R_{ref}} \cdot \cos[\varphi(x, y) + \psi_2] \end{array} \right\}$$
(3)

Here I_1 and I_2 are the detected intensities on the camera for the first and second bright-field images, respectively; I_0 is the photon flux of illumination, R_{inc} is the 'incoherent' reflectivity from all the sample structures and optical system parts, $R_{coh-sam}(x, y)$ is the 'coherent' reflectivity from all sample structures lying within the coherence volume, R_{ref} is the reflectivity from the reference mirror, $\varphi(x, y)$ is the phase difference between the sample and reference signals (denoting fringes in the 2D image), ψ is the additional phase, determined by the axial position of the reference mirror. The latter is typically changed by modulation with a piezoelectric motor. By modulating the piezo motor with a step-like function that: (1) keeps the phase constant during the acquisition of each camera frame and (2) has an amplitude of π ,

one can reject the ‘incoherent’ light as given below

$$I_1(x, y) - I_2(x, y) = \frac{I_0}{2} \sqrt{R_{coh-sample}(x, y) \cdot R_{ref}} \cos[\varphi(x, y)] \quad (4)$$

Taking a square and keeping the non-homogeneous (dependent on x, y) terms, we get

$$[I_1(x, y) - I_2(x, y)]^2 = \text{constant} \cdot R_{coh-sample}(x, y) \cdot \cos^2[\phi(x, y)] \quad (5)$$

As one can notice, although the two-phase demodulation scheme produces an optical section, it cannot demodulate the interference into the perfectly separate amplitude and phase components – Equation (5) contains reflectivity amplitude $R_{coh-sample}(x, y)$ but also the phase component $\varphi(x, y)$. The latter is responsible for interference fringe artifacts that are degrading the TD-FF-OCT images, particularly images from the uniform reflecting layers (such as corneal endothelium).

Other phase schemes allow complete demodulation of interference into amplitude and phase components but require more bright-field images. In the case of four-phase modulation, we get

$$\begin{aligned} I_1(x, y) &= \frac{I_0}{4} \cdot \left\{ \frac{R_{inc} + R_{coh-sample} + R_{ref} +}{2 \cdot \sqrt{R_{coh-sample} \cdot R_{ref}}} \cdot \cos[\varphi(x, y) + 0] \right\} \\ I_2(x, y) &= \frac{I_0}{4} \cdot \left\{ \frac{R_{inc} + R_{coh-sample} + R_{ref} +}{2 \cdot \sqrt{R_{coh-sample} \cdot R_{ref}}} \cdot \cos\left[\varphi(x, y) + \frac{\pi}{4}\right] \right\} \\ I_3(x, y) &= \frac{I_0}{4} \cdot \left\{ \frac{R_{inc} + R_{coh-sample} + R_{ref} +}{2 \cdot \sqrt{R_{coh-sample} \cdot R_{ref}}} \cdot \cos\left[\varphi(x, y) + \frac{\pi}{2}\right] \right\} \\ I_4(x, y) &= \frac{I_0}{4} \cdot \left\{ \frac{R_{inc} + R_{coh-sample} + R_{ref} +}{2 \cdot \sqrt{R_{coh-sample} \cdot R_{ref}}} \cdot \cos[\varphi(x, y) + \pi] \right\} \end{aligned} \quad (6)$$

Then the amplitude and phase can be retrieved as

$$\begin{aligned} A &= \sqrt{(I_3 - I_1)^2 + (I_4 - I_2)^2} \sim \sqrt{R_{coh-sample}} \\ \Phi &= \arctan\left(\frac{I_4 - I_2}{I_3 - I_1}\right) \end{aligned} \quad (7)$$

The latter demodulation method is free from interference artifacts.

Sensitivity

Sensitivity is defined by the smallest signal that can be detected with TD-FF-OCT [when the signal-to-noise ratio (SNR) = 1]⁴⁴

$$R_{min} \sim \left(\frac{\xi_{sat} + \chi^2}{N \xi_{sat}^2} \right) \cdot \frac{(R_{ref} + R_{inc})^2}{R_{ref}} \quad (8)$$

where R_{min} is the minimum detectable reflectivity at SNR = 1, ξ is the full-well capacity (FWC) of the camera, χ is the electric noise of the camera, and N is the number of averaged TD-FF-OCT images.

The above Equation (8) can be understood intuitively. The camera in TD-FF-OCT acquires bright-field images. The detected light contains interference signals that denote themselves by the small brightness variations on top of the much brighter incoherent background. The high FWC allows for detection of more photons and better resolves the intensity variations in the bright scene (better sensitivity). It is interesting to note that the dynamic range is a much less important parameter. Indeed, the high dynamic range makes the device sensitive to variations between the dark and bright pixels, but less to small brightness variations in the bright scene.

For FF-OCT, there are usually two ways to improve the sensitivity. One is to increase the FWC of the camera, while the other method is to use a reference mirror with a similar reflectance to the total reflectance of the incoherent light in the optical system. Typically, biological samples have reflectivity below 10%. For example, corneal reflectivity is ~2% [determined by Snell’s law and refractive indexes of the air (1.0) – corneal tear

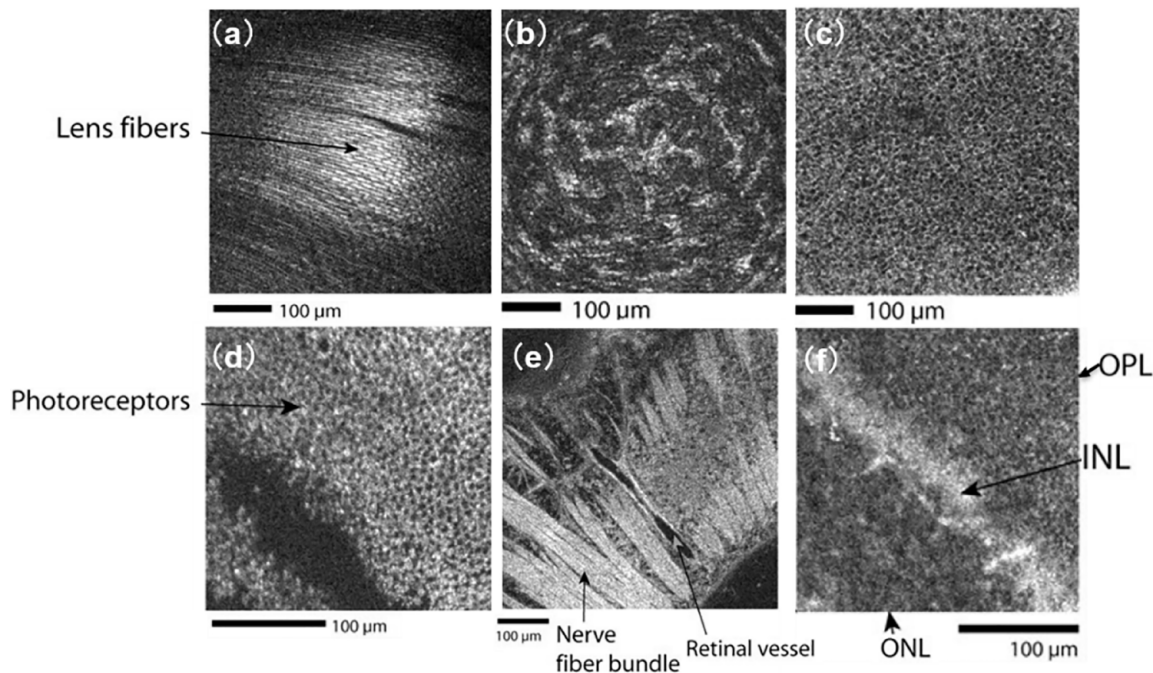


Figure 2. *Ex vivo* full-field OCT imaging of animal ocular. (a–c) Anterior segment of a mouse eye. (a) The raw image inside the anterior cortex, (b) keratocytes, and stromal fibers, (c) tightly packed epithelial cells. (d–f) *Ex vivo* full-field OCT imaging of rodent and porcine retina samples. (d) Pig photoreceptors, (e) the nerve fiber bundles in the rat retina, and (f) image showing the rat plexiform and nuclear layers.

Source. Adapted from the study by Grieve *et al.*⁵⁰

INL, inner nuclear layer; ONL, outer nuclear layer; OPL, outer plexiform layer.

film (1.336) interface]. A close refractive index of 4% can be achieved by using the glass reference mirror. Finally, averaging TD-FF-OCT images reduces the noise and improves sensitivity.

TD-FF-OCT in ex vivo and animal ophthalmic studies

At the time of its introduction in 1998, TD-FF-OCT was limited to studies of *ex vivo* static samples, as no high-speed high-SNR cameras were available at that time. Nevertheless, *ex vivo* biological and medical research saw a great value in a micron-level resolution introduced by TD-FF-OCT as it enabled rapid histological evaluation of *ex vivo* tissue samples and brain tissue characterization,^{50–56} the study of embryology and developmental biology,^{57–59} and so on. The particular interest attracted the morphological visualization of ophthalmic tissues (cornea and retina) aspiring to bring both a deeper scientific understanding of the eye function and help patients in clinics (for example, by evaluating the quality of the transplantable corneal grafts).

Ex vivo imaging of animal eyes

To open possibilities for *ex vivo* studies, an adaptation of the original TD-FF-OCT architecture was required. In 2004, Dubois *et al.*⁶⁰ replaced the original design utilizing polarized optics and photo-elastic modulator for phase-shifting with the new design using non-polarized optics and piezo-mirror in the reference arm.

The same year, Grieve *et al.*⁵⁰ applied the new TD-FF-OCT design for studying the structure of anterior and posterior eyes *ex vivo* for the first time (Figure 2). *Ex vivo* mouse, rat, and porcine eye samples were under the study. The work used the slow CCD camera with a frame rate of 15 frames per second (FPS) – sufficient for studying the *ex vivo* samples. Phase modulation was achieved by moving the reference mirror with a piezo-electric actuator. The light source was a tungsten-halogen lamp with a visible central wavelength of 770 nm and broad spectral range of 350 nm. The latter resulted in the sub-micron 0.7 µm axial resolution in tissue. At the same time, microscope objectives with NA of 0.3 (10×)

or 0.5 (20 \times) were provided lateral resolutions of 1.4 and 0.8 μm , respectively. The microscope objectives were water immersion to reduce the specular reflection from the sample surface and increase the interference contrast. Thus, the system was in contact. Due to the low FWC of the camera used, the final TD-FF-OCT image was reconstructed after accumulating (averaging) 5–10 images. The time of 1 s required to produce an en face tomographic image was greatly faster compared with the time required for cross-sectional scanning OCT at that time.

The images revealed cell-level details in the rat and mouse corneas. Few microns large epithelial and stromal keratocyte cells in the cornea, as well as fibers in the lens of the eye, were clearly resolved in en face views. Cross-sectional images, reconstructed from the stack of en face images have also shown a great level of detail: different epithelial layers, Bowman's membrane, stroma, Descemet's membrane, aqueous humor, lens capsule, lens epithelial cells, and cortical lens fibers could be resolved in the anterior eye.

In addition to corneal images, the researchers also obtained retinal images. They removed the anterior segment from the whole eye and lowered the microscope objective directly into the vitreous. In the rodent and porcine retina samples, many layers were visible in cell detail, including: photoreceptor layer (PRL), external limiting membrane (ELM), outer nuclear layer (ONL), outer plexiform layer (OPL), inner nuclear layer (INL), inner plexiform layer (IPL), ganglion cell layer (GCL), nerve fiber layer (NFL), outer segment (OS), inner segment (IS), as well as retinal pigmental epithelium (RPE), Bruch's membrane, choroid, and sclera.

This work highlighted the importance of en face views that were rarely used in OCT and histology at that time. While cross-sectional imaging was best suited for evaluating the thickness of the retinal layers, en face views could be used to measure the cellular organization.

Ex vivo imaging of human donor eyes

In 2007, Akiba *et al.*⁶¹ reported the first subcellular imaging of a human donor cornea and the visualization of a 2D keratocyte network by TD-FF-OCT. In their study, TD-FF-OCT provided en face images that could delineate the morphological features of a human cornea at a

subcellular level. Corneal epithelium, keratocytes in stroma, and endothelium were clearly observed.

Later in 2015, Ghouali *et al.*⁶² has shown the value that high-resolution imaging of TD-FF-OCT can bring to clinics (Figure 3). *Ex vivo* corneas from healthy human subjects were compared with the corneas from human patients affected with various pathologies. The commercial TD-FF-OCT device (LightCT, LLTech, Paris, France) that was used had similar characteristics as the experimental device described above, and also had an added easy-to-use interface. TD-FF-OCT could detect corneal edema, abnormalities caused by pathologies such as keratoconus, keratitis, and Fuch's endothelial dystrophy. Each condition could be distinguished from one another by: (1) checking the depth of the corneal layer affected, (2) measuring the density of corneal cells, (3) checking for deposits and inclusions in the tissue, (4) checking the global/local corneal opacification, and (5) irregularity in the thicknesses of corneal layers. The cornea is a transplantable tissue. In this context, the mentioned study is particularly valuable, as it provides an additional high-detailed way to examine the health of corneal transplants. Thus, potentially providing a better outcome for the patient following the surgery. Moreover, no tissue preparation, modification, or staining of any kind is required for TD-FF-OCT imaging, which makes it potentially suitable for use in corneal banks.

In 2015, Grieve *et al.*⁶³ created a new device that combined TD-FF-OCT with fluorescence confocal microscopy (FCM) to gain more biological insights into the *ex vivo* human retina (Figures 4 and 5). TD-FF-OCT device was specially adapted for high-resolution imaging: (1) water immersion microscope objectives had 0.8 NA leading to 1.6 μm lateral resolution, (2) CMOS camera had an increased FWC of 200 ke leading to higher sensitivity to interference contrast variations. The resolution down to the single cell and single axon provided one of the most detailed optical tomographic images of the retina at that time.

In 2019, Bocheux *et al.*⁶⁴ showed that commercial TD-FF-OCT devices (LightCT, LLTech, Paris, France) can quantitatively measure corneal transparency. This makes the device promising as a screening test for corneal grafts to determine their suitability as transplants.

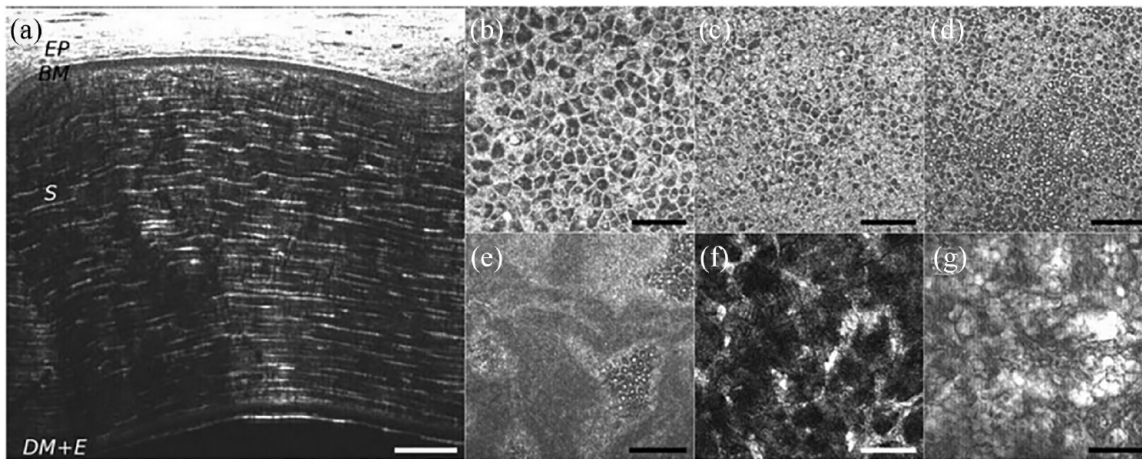


Figure 3. Organ-cultured normal cornea after de-swelling in a dextran-containing medium. (a) Cross-sectional slice with marked layers; EP, epithelium (38 mm thick); BM, Bowman's layer (11 mm thick); S, stroma (510 mm thick); DM + E, Descemet's membrane (10 mm thick) and endothelium. (b–g): 'En-face' images. (b) Superficial epithelial layer; (c) wing cell layer; (d) basal epithelial layer; (e) basal epithelial cells, basement membrane (hyper-reflective zones), and Bowman's layer (hypo-reflective zones). (f) Stromal keratocytes and lamellae of collagen bundles. (g) Endothelial cells were revealed by decreasing axial resolution (sum of ten 1 mm thick slices). The bar shows 70 mm in (a) and 100 mm in (b–g). Reproduced from the study by Ghouali *et al.*⁶² (www.tandfonline.com).

A notable attempt at the first *in vivo* TD-FF-OCT imaging was performed by Grieve *et al.*⁶⁵ back in 2005. They used a maximum repetition rate of 250 Hz to obtain images of the anterior eye of anesthetized rats in 4 ms and obtained tomographic images of different corneal and lens layers. This result was important as a proof of concept of *in vivo* imaging; nevertheless, the possibility of applying the device for an examination of *in vivo* human eye was a long way beyond the reach of the device. More precisely, the instrument used white light illumination that is known to introduce strong visual discomfort. The use of white light also brings the risk of photochemical damage to the retina in addition to the thermal one, defined by the ISO 15004-2:2007 standard. The xenon arc lamp light source was emitting continuous illumination that could not be pulsed to assure the ocular safety (by decreasing the power absorbed by the ocular tissues over time). The water-immersion objectives increased the image contrast, however, made the instrument contact impractical for use in humans.

TD-FF-OCT for corneal elastography

In 2013, Nahas *et al.*⁶⁶ produced an elastography image of the cornea by correlating the TD-FF-OCT volumes before and after the controlled

deformation. The strain of the epithelium layer was found to be about two times larger than that of the stroma.

Dynamic TD-FF-OCT

In 2016, Apelian *et al.*⁶⁷ introduced a new contrast imaging method that relies on the live activity of cells. The method is based on the principle that small movements of intracellular organelles can substantially shift the interferometric fringes (or change their contrast). By acquiring a time-stack of TD-FF-OCT images, one can assign the frequency of pixel modulation to one channel of the colormap (H), the standard deviation of the frequency to the second channel (S), and the cumulative signal sum to the third channel (V). Thus, the method produces a colored TD-FF-OCT image, where color is connected to live activity. This label-free contrast method was named dynamic TD-FF-OCT.

Regarding ophthalmic imaging, Scholler *et al.*⁶⁸ obtained impressive images of retinal organoids using dynamic TD-FF-OCT. The method opens a new window of opportunities for understanding the biological processes inside the cells and functions of individual organelles.

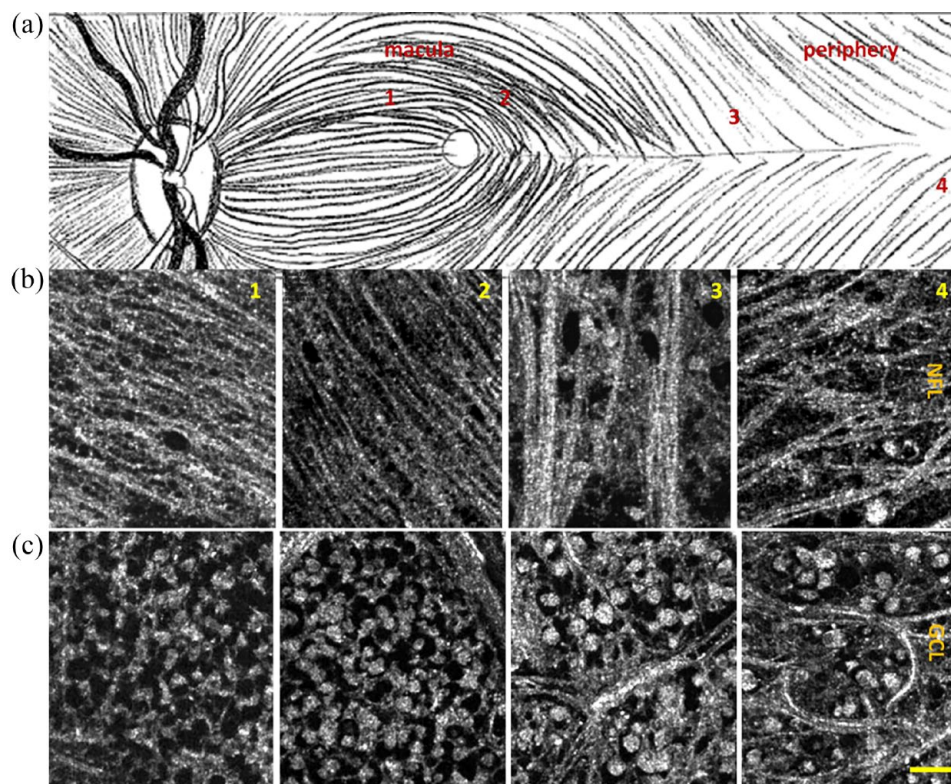


Figure 4. Full-field OCT images of human *ex vivo* retina. (a) Illustration of the fundus showing raphe median region running from macula to periphery. One through four indicate approximate zones of en face images in row (b) NFL and row (c) GCL. Scale bar: 50 μm . Republished from the study by Grieve *et al.*⁶³

The dynamic method is also useful to follow wound-healing process in *ex vivo* corneas and retinas (Figure 6).⁶⁹ This method allows to measure the cell migration speed and follow the metabolic activity of the cells around the wound.

TD-FF-OCT in human eyes *in vivo*

First in vivo human corneal and retinal imaging

The first TD-FF-OCT imaging of *in vivo* human eye was achieved in 2018 by Mazlin *et al.*⁷⁰ and Xiao *et al.*⁷¹ Part of the success was due to the use of the new custom-made camera with a high FWC of 2Me – about 10 times larger than existing alternatives. This allowed to collect more photons per frame and have a higher sensitivity to small light intensity variations (interference signals) within the bright scene. As a drawback, this required sending more photons into the eye and additional work to ensure ocular safety. High-intensity illumination was achieved by using a high-power LED with a small chip about the size

of the imaged area, thus ensuring the effective coupling of the light from the source. The LED was triggered in a pulsed mode (typical pattern: 3.5 ms illumination, 100 ms no illumination), to keep the power way below the maximum permissible irradiance specified by ISO and ANSI light safety standards. Illumination from the LED with a wavelength of 850 nm was comfortably visible as a dim red circle due to the low sensitivity of the retina to near-infrared (NIR). The air microscope objectives made the instrument non-contact (2 cm between the eye and device).

The corneal and retinal imaging systems had a few differences. In the corneal imaging system, the reference mirror was a neutral density glass filter, producing the 4% light reflection only from the front glass surface. This reflectivity was selected to be close to 2% from the air tear-film interface to ensure the highest sensitivity. In retinal imaging devices, which used optics of the eye (cornea, lens) for focusing, the reflectivity of the retina was insufficient to saturate the camera. To

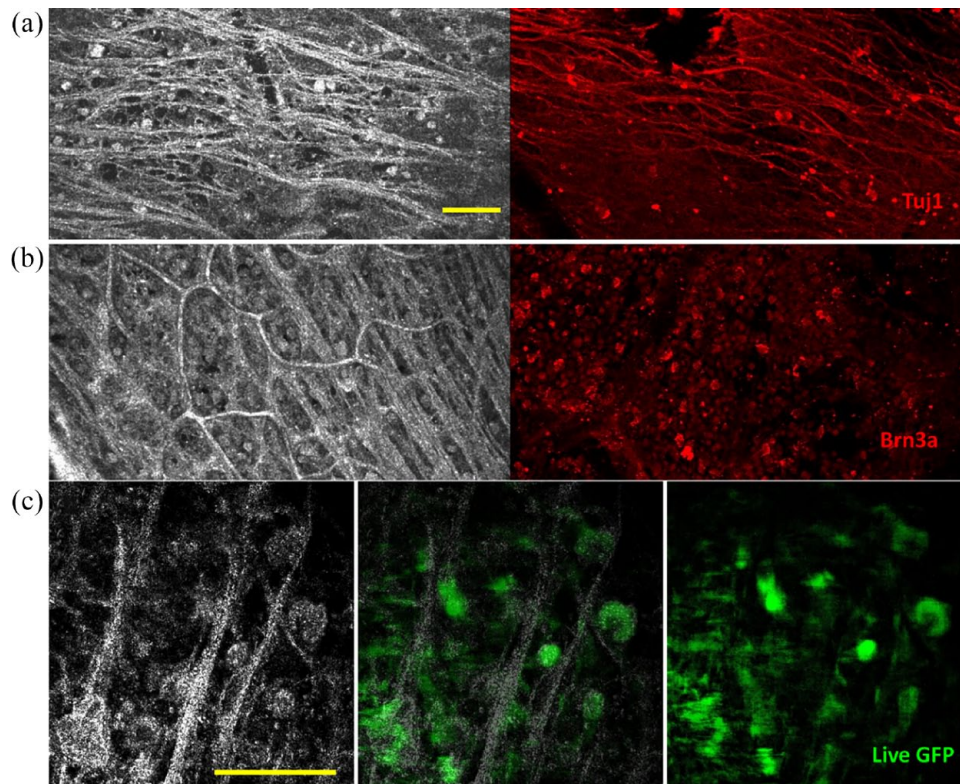


Figure 5. Full-field OCT and FCM in humans and fluorescence-FF-OCT in primates. (a, b) Full-field OCT (left) and FCM (right) images of the human retina, in subject three. (a) Sparse axons and cells at periphery visible as hyperreflective structures in FF-OCT (left) and similar region with FCM labeled with Tuj1 (red), which labels ganglion and amacrine cell somas and axons; (b) densely packed cells in GCL in a location closer to the optic nerve, where cells, nerve fibers, and capillaries are visible as hyperreflective structures in FF-OCT (left) and in the similar region with FCM (right) where ganglion cell nuclei are labeled with Brn3a (red). (c) Full-field OCT (left) combined fluorescence-FF-OCT (center) and fluorescence (right) images of GFP-labeled RGC somas in live macaque retina using fluorescence-FF-OCT, with pixel to pixel overlay. Scale bars: 100µm. Reproduced from the study by Grieve *et al.*⁶³

ensure saturation, the reference mirror with a higher reflectivity (Aluminum – 30%) was installed (Figure 7).

Corneal and retinal imaging also introduced unique challenges compared with *ex vivo* imaging. The difference between the refractive indexes of air and the eye introduced an optical mismatch between the interferometric arms. More precisely, when imaging inside the sample, the DOF was extended deeper in the sample (due to Snell's law) and was not matching to the location of the sectioned slice, resulting in a loss of the signal. This problem was particularly critical for corneal imaging, as the microscope objective in the sample arm had high NA and small DOF (while the NA for the retinal imaging was smaller, determined by the

diameter of the pupil of the eye). This problem called defocus was well known before the study by Blavier *et al.*⁷² and had a solution – the deeper the DOF inside the sample, the more the reference arm of the interferometer should be extended to recover the optical matching. Corneal imaging could be achieved by pre-setting the reference arm position to the slice of interest (for example, endothelium). The eye was moving randomly axially and occasionally ending up in the position where the focus was also at the endothelium layer, thus producing a tomographic image. The influence of axial eye motion can be corrected by some methods, including correction algorithm or hardware improvement.^{73,74} TD-FF-OCT chose the latter to correct axial eye movement by combining SD-OCT.

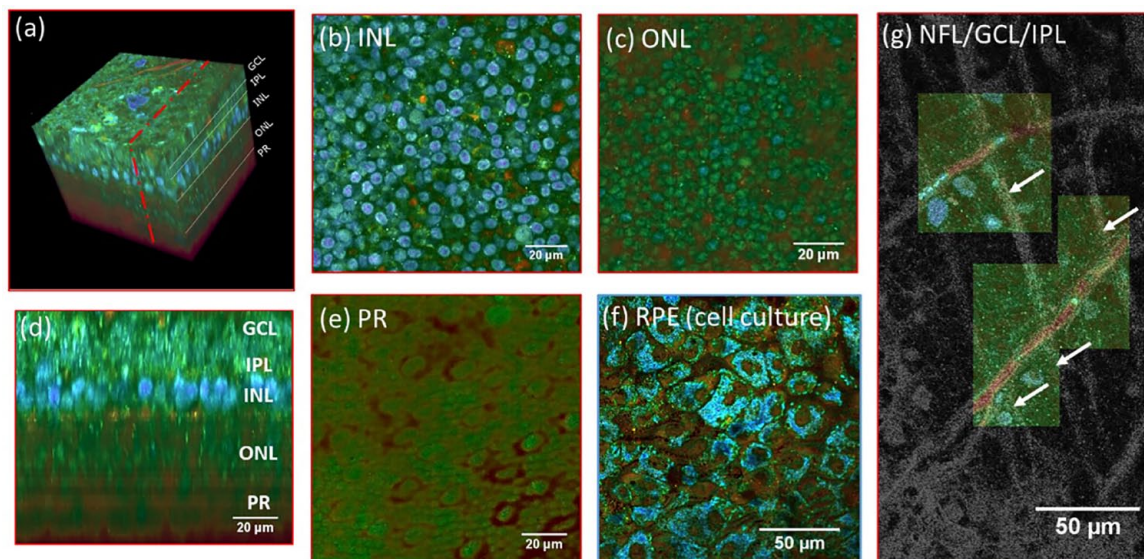


Figure 6. (a) 3D reconstruction of a D-FF-OCT image stack in explanted macaque retina over a 120 by 120 μm field of view. (b, c, e) En-face images of the (b) inner nuclear layer, (c) outer nuclear layer, and (e) photoreceptor layer. (d) Reconstructed cross-section at the location represented by the red dotted line in (a). The cross-section in (d) was linearly interpolated to obtain a unitary pixel size ratio. (f) D-FF-OCT image of a porcine retinal pigment epithelium cell culture. (g) Overlay of colored D-FF-OCT and FF-OCT at the interface between the layers of the nerve fibers (white arrows point to nerve bundles that are very bright in static and invisible in dynamic mode), ganglion cells (blue and green cells, visible in dynamic mode), and inner plexiform (fibrous network, bottom left, visible in static mode). Samples were maintained *in vitro* in a culture medium at room temperature during imaging. Reproduced from the study by Scholler *et al.*⁶⁹

The first combined TD-FF-OCT + SD-OCT system was introduced by Xiao *et al.*⁷⁵ with the purpose to locate the retina through the SD-OCT cross-sectional image. This was important because retinal signals in a single TD-FF-OCT image were too low. A high-quality retinal image can be reconstructed from a stack of TD-FF-OCT images; however, one can acquire a stack only once per several seconds to ensure light safety. SD-OCT can provide information about the retinal position in real time without turning on TD-FF-OCT. Only when the retina is in the correct position, the user turns on the TD-FF-OCT illumination and collects the stack of images (Figure 8).

The two devices have shown that TD-FF-OCT can obtain cell resolution images in the live human eye. In the cornea, one could resolve tear film reflection, epithelium, few micrometer-thick sub-basal nerves, Bowman's membrane, 15 μm keratocyte cell nuclei in the stroma, Descemet's membrane, and 20 μm hexagonal endothelial cell mosaic. Although corneal imaging with detail was possible using clinical *in vivo* confocal microscopy,

TD-FF-OCT provided additional benefits of non-contact operation as well as larger FOV (~16 times in terms of area). In the retina, TD-FF-OCT resolved retinal nerve fibers as well as individual photoreceptors. It is particularly curious that this level of detail was achieved without using any correction of ocular aberrations that typically degrade the images even from healthy eyes. Xiao *et al.*⁷⁶ exposed this phenomenon, their study showed that full-field interferometry with incoherent illumination is less sensitive to optical aberrations compared with conventional microscopy. More precisely, the symmetric optical aberrations are less detrimental to the resolution but reduce the signal. This effect was later studied by Blavier *et al.*⁷² and Barolle *et al.*⁷⁷ The latter rigorous publication has shown that the spatial incoherence of the illumination acts as a virtual confocal pinhole in TD-FF-OCT and its imaging performance is equivalent to a scanning time-gated coherent confocal microscope (CM). Thus, TD-FF-OCT had nearly twice the resolution of standard imaging at a moderate aberration level. It has shown to be particularly robust to low-order symmetric aberrations (such as defocus).

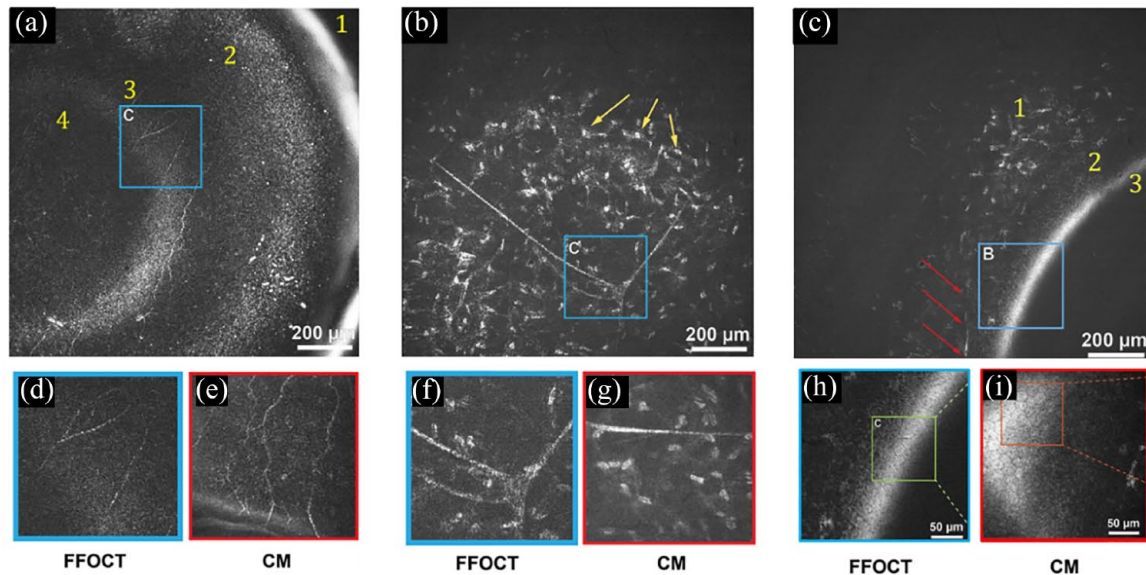


Figure 7. *In vivo* anterior human cornea images were obtained with FF-OCT and CM. (a) FF-OCT images of the anterior cornea at different depths. 1 – strong reflection on air–tear film interface, 2 – epithelium, 3 – SNP with nerves clearly seen, 4 – Bowman's layer. (b) *In vivo* human corneal images of middle stroma, yellow arrows show the stromal nerves. (c) FF-OCT image of the posterior cornea. 1 – posterior stromal keratocytes, 2 – Descemet's membrane; 3 – endothelium. A nerve is shown by the red arrows. (d, f, and h) zoomed areas ($300\ \mu\text{m} \times 300\ \mu\text{m}$) of (a), (b), and (c). (e, g, and i) Confocal microscopy images ($300\ \mu\text{m} \times 300\ \mu\text{m}$) of the same area of (d), (f), and (h). Republished from the study by Mazlin *et al.*⁷⁰

Improving in vivo TD-FF-OCT: real-time, high-signal, and large FOV imaging

Next efforts largely focused on making TD-FF-OCT imaging reliable to be more suitable for clinical studies in patients. Mazlin *et al.*⁷⁸ improved the combined TD-FF-OCT + SD-OCT device above by making an automatic corneal position tracking with SD-OCT and fast defocus correction with a voice coil motor in the reference arm. The device could correct eye movements at 50 Hz with a correction error of about $10\ \mu\text{m}$, producing images from the cornea in real time. No manual layer-by-layer correction was needed. The new device also simplified imaging of the other anterior eye layers. In limbus, it could resolve the palisades of Vogt, a hosting area for stem cells of the eye, as well as view and quantify the blood flow (angiography). Tear film could be clearly seen and its flow velocity could be quantified – a potentially important biomarker for spread-in-population dry eye disease.

The same principle of eye tracking with SD-OCT and correction with a voice coil motor in the reference arm was adapted by Mecê *et al.*⁷⁹ for retinal imaging. However, the difference is that the correction was not used for defocusing (required

in the cornea), but for fixating on a single retinal layer. Prolonged acquisition from the same retinal layer could be averaged in time to improve SNR.

From the signal standpoint, single TD-FF-OCT images contained enough signal to resolve all corneal layers; however, signals in the single retinal images were weak (due to the smaller number of back-scattered ballistic photons from the retina as well as the smaller NA provided by the eye) and required heavy averaging. Scholler *et al.*⁸⁰ implemented an additional compact defocus-correcting lens that allowed to considerably improve the retinal images.

Another recent direction of work focused on improving the FOV. From the start, TD-FF-OCT systems provided a relatively large FOV of about 1 mm, which was on par or better than other cell-resolution clinical machines (for example, *in vivo* confocal microscopy; Figure 9).^{81–85} However, due to the curvature of the cornea, this FOV was sectioning through several corneal layers at once, effectively reducing the visible FOV of each individual layer. Mazlin *et al.*⁸⁶ adapted the shape of the optical sectioning field to the shape of the cornea by installing the curved lens into the reference arm. This allowed unprecedented FOV of the

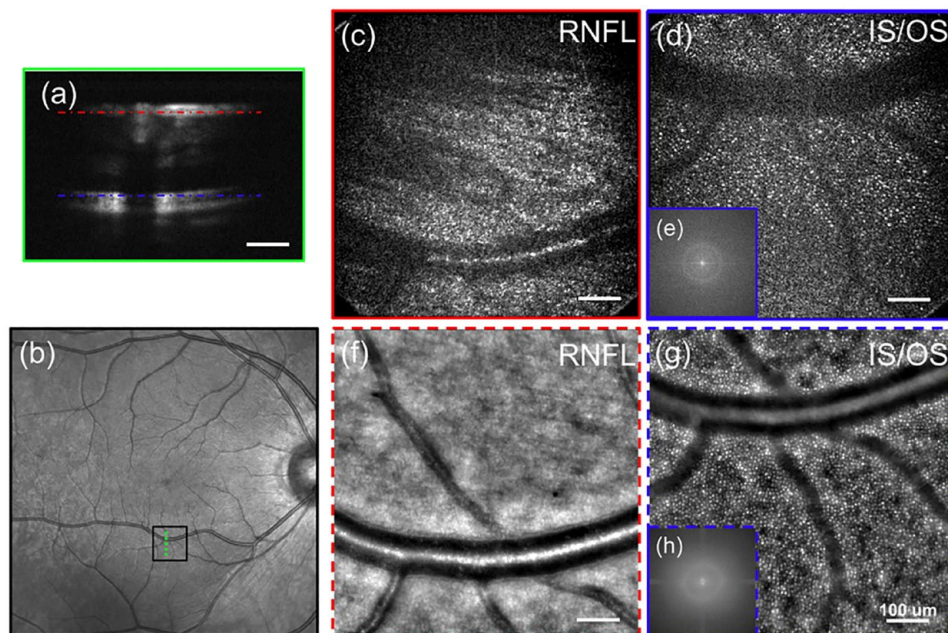


Figure 8. *In vivo* human retinal imaging by (c, d) FF-OCT compared with (f, g) AO retinal camera of the near periphery at 6° eccentricity. (a) The SD-OCT cross-sectional image of the imaging position with the red (RNFL) and blue (IS/OS) dashed lines indicates the FF-OCT imaging depth. (b) Fundus photography with the black box indicating the FF-OCT imaging area and the green dashed line showing the SD-OCT scanning position. *In vivo* FF-OCT image at 6° inferior to the fovea at the (c) RNFL and (d) IS/OS photoreceptor layer without AO. (e) The 2D power spectra of (d) show the Yellot's ring, the radius of which is related to the cone photoreceptor spacing. The AO retinal camera image around the (f) RNFL and (g) IS/OS photoreceptor layer at the same retinal location, and (h) the 2D power spectra of (g). Scale bar: $100\ \mu\text{m}$. Republished from the study by Xiao *et al.*⁷¹

corneal sub-basal nerve and endothelial layers. Much more nerves and cells can be counted potentially leading to a more precise quantitative diagnosis of corneal conditions.

A similar approach to shaping the optical coherence gate was adapted by Mecê *et al.*⁸⁷ in retinal imaging. However, as the retinal curvature was smaller than that of the cornea, installing a glass plate was sufficient to flatten the retinal FOV.

Alternative holographic FF-OCT

Interestingly, in 2016, Sudkamp *et al.*⁸⁸ presented a full-field system that used a different approach to acquire en face images of *in vivo* human retina. Instead of acquiring several phase-shifted images in time, the mentioned approach captured them in a single shot using a holography-like approach. More precisely, the device used a fixed tilted reference mirror, a coherent super luminescent diode (SLD) light source to acquire the interference speckled pattern that, being filtered in Fourier domain, produced an en face section. By scanning the reference mirror, volumetric retinal

images could be acquired. Simplicity is an undeniable advantage of the above method; however, it comes with a cost of reduced FOV (required for Fourier processing) and relatively low resolution (similar to the conventional clinical OCT).

Future directions of ophthalmic TD-FF-OCT

Matrix-based FF-OCT

Imaging through scattering cornea or crystalline lens presents a big challenge for ophthalmic diagnosis. Particularly so because the conditions leading to scattering are common in the population (for example, cataracts and corneal scarring). OCT and FF-OCT methods that discriminate ballistic photons from the multiple-scattering background are both negatively affected by the excessive scattering as it reduces the number of single-scattered photons. The smart OCT approach, which improves upon the TD-FF-OCT optical design, was introduced by Badon *et al.*⁸⁹ The method aims to overcome the multiple scattering problem by measuring the reflection matrix of the sample and then removing the

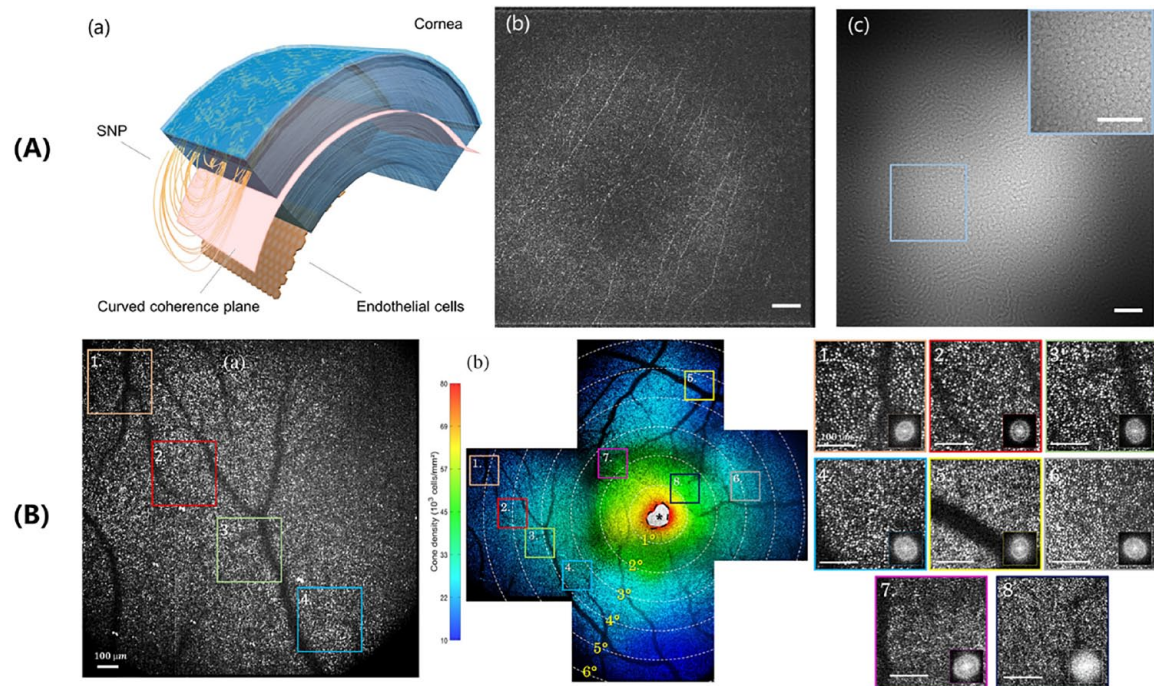


Figure 9. A: Curved-field OCT imaging of the SNP and endothelium in the human cornea *in vivo*. By matching the curvature of optical sectioning with the curvature of the cornea, CF-OCT substantially increases the FOV of the corneal endothelial layer. All scale bars are 0.1 mm. Adapted from the study by Mazlin *et al.*⁸⁶ B: Adaptive-glasses time-domain FF-OCT for wide-field high-resolution retinal imaging, the highest three-dimensional (3D) resolution possible in *in vivo* retinal imaging is achieved by combining optical coherence tomography (OCT) and adaptive optics. (a) $5^\circ \times 5^\circ$ FOV FF-OCT retinal image, (b) $12^\circ \times 12^\circ$ FOV image after stitching together five FF-OCT images. Zoomed areas of $1^\circ \times 1^\circ$ FOV, chosen to be representative of different eccentricities, and their respective Fourier transforms are also shown. Adapted from the study by Scholler *et al.*⁸⁰

multiple-scattering contribution through matrix processing. The reflection matrix is constructed by illuminating each first point of the sample and then detecting the photons from each second point of the sample (optionally first and second points can be the same). Although this method allows twice as much deeper imaging compared with OCT, substantial time is required for the acquisition and reconstruction of the reflection matrix. Therefore, today's applications are limited to *ex vivo* studies.

Dark-field TD-FF-OCT

A series of publications by Aukorius and Boccara^{90,91} demonstrated dark-field TD-FF-OCT, where an opaque disk placed in the pupil plane was used to block the specular reflections and increase the tomographic image contrast. The results from the human fingerprint imaging suggest that this method can be also applied to gain imaging contrast in other *in vivo* tissues such as the human eye.

Dynamic *in vivo* TD-FF-OCT

Dynamic TD-FF-OCT mentioned above was limited to *ex vivo* studies. However, there is a great interest to apply the method to *in vivo* eye, thus gaining not only the light scattering OCT contrast but also physiological information on how well the different layers of the eye function. Application of the dynamic method to *in vivo* eye is complicated by the movements of the eye that have a much greater amplitude than the desired intracellular movements. This task is seen as even more challenging if one remembers that the timescale during which the organelles move (tens of milliseconds to a second)⁶⁷ is long enough so that eye can move by many micrometers.⁹² However, there is a hope that the acquisition of a long stack of TD-FF-OCT images from the same ocular layer coupled with sophisticated 3D image processing may give access to dynamic information. In 2019, Scholler⁹³ showed that singular value decomposition (SVD) processing of the stacked TD-FF-OCT images can suppress the breathing and heart-beat artifacts

when imaging *in vivo* mouse liver. In this study, the mouse was anesthetized and attached to the water immersion microscope objective via the vacuum pump to suppress the movements. Application of this method to freely moving *in vivo* human eye will require substantial progress in both the imaging and processing parts.

Discussion

TD-FF-OCT is likely to have a significant impact on future ophthalmic imaging due to its non-contact, wide-field, and cellular-resolution nature. Indeed, the demand for en face imaging inspires extensive research to improve the speed of classical scanning OCT. Traditional OCT needs to obtain 3D images to retrieve en face views. However, even the fastest scanning OCT system is unlikely to reach en face imaging speed of TD-FF-OCT any time soon.

Therefore, in the en face view, compared with the traditional scanning OCT, the TD-FF-OCT will have fewer motion artifacts and higher time accuracy to monitor the dynamic process. With swept-source laser, Fourier-domain FF-OCT

(FD-FF-OCT; or the so-called full-field swept-source OCT) has also been developed achieving fast cellular imaging speed in both corneal and retinal imaging, however, suffers cross-talk noise that could degrade the image quality.^{30,94–96} Nevertheless, compared with Fourier-domain OCT techniques, TD-FF-OCT has relatively lower sensitivity. There are other excellent cellular imaging systems in the field of ophthalmic imaging. CM has been applied for cellular corneal imaging, which has improved the understanding of human corneal structure and pathophysiological mechanisms associated with various corneal diseases.^{82,83} However, its contact nature and the use of surface anesthetics and viscous gels during the examination may not only pose a risk of infection, but may also lead to changes in the corneal surface.⁸⁵ Adaptive optics (AO) assisted imaging systems such as AO retinal camera or AO-OCT-induced AO module for ocular aberration correction, achieving cellular resolution in human retinal imaging,^{97,98} but the system complexity and stability have limited their wide use in ophthalmic clinics. Table 1 summarizes the parameters and characteristics of representative ophthalmic imaging modalities.

Table 1. Comparison of TD-FF-OCT with other systems in *in vivo* imaging.

Reference	Technology	Resolution(μm)		Speed (FPS) ^a	Field of view (mm×mm)
		Axial	Lateral		
Cornea					
Mazlin <i>et al.</i> ⁷⁸	TD-FF-OCT	7.7	1.7	300	1.26×1.26
Auksorius <i>et al.</i> ²⁴	FD-FF-OCT	5.6	2.4	20,000	0.615×0.615
Han <i>et al.</i> ⁹⁹	OCT	1.7	3	2500	0.7×1.4
Bohn <i>et al.</i> ¹⁰⁰	CM	8	1.5	30	0.266×0.286
Retina					
Scholler <i>et al.</i> ⁸⁰	TD-FF-OCT	8	3.9	300	1.5×1.5
Auksorius ⁹⁶	FD-FF-OCT	4.5	2	20,000	1.0×1.0
Ginner <i>et al.</i> ¹⁰¹	OCT	2.8	5.5	100	1.2×0.6
Liu <i>et al.</i> ¹⁰²	AO fundus camera	N/A	2.1	13.4	0.9×0.9

AO: adaptive optics; CM: confocal microscopy; FD-FF-OCT: Fourier-domain full-field optical coherence tomography; FPS: frames per second; OCT: optical coherence tomography ophthalmoscopy; TD-FF-OCT: time-domain full-field optical coherence tomography.

^aThe speed here refers to the speed of en face imaging.

Conclusion

In conclusion, through the non-invasive, wide-field planar imaging, the improvement of FF-OCT will improve our understanding of human eye physiology and pathology. The ultra-high axial resolution, lateral resolution, and three-dimensional imaging mode make FF-OCT more accurate in detecting the pathophysiological changes of the eyeball, which has great potential for basic and clinical application in ophthalmology.

Declarations

Ethics approval and consent to participate

Not applicable.

Consent for publication

Not applicable.

Author contributions

Jinze Zhang: Investigation, Visualization, Writing – original draft, Writing – review & editing.

Viacheslav Mazlin: Investigation, Visualization, Writing – original draft.

Keyi Fei: Formal analysis, Validation, Writing – review & editing.

Albert Claude Boccara: Formal analysis, Supervision, Validation, Writing – review & editing.

Jin Yuan: Conceptualization, Resources, Supervision, Validation, Writing – review & editing.

Peng Xiao: Conceptualization, Methodology, Project administration, Resources, Supervision, Writing – review & editing.

Acknowledgements

None.

Funding

The authors disclosed receipt of the following financial support for the research, authorship, and/or publication of this article: This research was supported by the National Natural Science Foundation of China (Grant Nos 82230033 and 82271133), the Department of Science and Technology of Guangdong Province (Grant Nos 2021TX06Y127

and 2021TQ06Y137), and the Basic and Applied Basic Research Foundation of Guangdong Province (Grant No. 2022A1515011486).

Competing interests

The authors declared no potential conflicts of interest with respect to the research, authorship, and/or publication of this article.

Availability of data and materials

Not applicable.

ORCID iD

Jinze Zhang  <https://orcid.org/0000-0002-4461-1095>

References

1. Fujimoto JG. Optical coherence tomography for ultrahigh resolution in vivo imaging. *Nat Biotechnol* 2003; 21: 1361–1367.
2. Izatt JA, Hee MR, Swanson EA, *et al.* Micrometer-scale resolution imaging of the anterior eye in vivo with optical coherence tomography. *Arch Ophthalmol* 1994; 112: 1584–1589.
3. McCabe JM and Croce KJ. Optical coherence tomography. *Circulation* 2012; 126: 2140–2143.
4. Lin HY, Zhang ZJ, Markl D, *et al.* A review of the applications of OCT for analysing pharmaceutical film coatings. *Appl Sci-Basel* 2018; 8: 2700.
5. Tan B, Hosseinaee Z, Han L, *et al.* 250 kHz, 15 μm resolution SD-OCT for in-vivo cellular imaging of the human cornea. *Biomed Opt Express* 2018; 9: 6569.
6. Chen VM, Mehta N, Robbins CC, *et al.* Anterior-segment spectral domain optical coherence tomography in epidermolysis bullosa. *Ocul Surf* 2020; 18: 912–919.
7. Sadda SR, Abdelfattah NS, Lei J, *et al.* Spectral-domain OCT analysis of risk factors for macular atrophy development in the HARBOR study for neovascular age-related macular degeneration. *Ophthalmology* 2020; 127: 1360–1370.
8. Marchand PJ, Riemensberger J, Skehan JC, *et al.* Soliton microcomb based spectral domain optical coherence tomography. *Nat Commun* 2021; 12: 427.
9. Yang S, Gao Z, Qiu H, *et al.* Low-reflectivity drusen with overlying RPE damage revealed by

- spectral-domain OCT: hint for the development of age-related macular degeneration. *Front Med (Lausanne)* 2021; 8: 706502.
10. Yaqoob Z, Wu J and Yang C. Spectral domain optical coherence tomography: a better OCT imaging strategy. *Biotechniques* 2005; 39(6, Suppl.): S6–S13.
 11. Dysli M, Rückert R and Munk MR. Differentiation of underlying pathologies of macular edema using spectral domain optical coherence tomography (SD-OCT). *Ocul Immunol Inflamm* 2019; 27: 474–483.
 12. Wang J and Yin LR. The application of enhanced depth imaging spectral-domain optical coherence tomography in macular diseases. *J Ophthalmol* 2020; 2020: 9503795.
 13. Lim LS, Mitchell P, Seddon JM, *et al.* Age-related macular degeneration. *Lancet* 2012; 379: 1728–1738.
 14. Mitchell P, Liew G, Gopinath B, *et al.* Age-related macular degeneration. *Lancet* 2018; 392(10153): 1147–1159.
 15. Chakravarthy U and Peto T. Current perspective on age-related macular degeneration. *JAMA* 2020; 324: 794–795.
 16. Chopra R, Wagner SK and Keane PA. Optical coherence tomography in the 2020s—outside the eye clinic. *Eye (Lond)* 2021; 35: 236–243.
 17. Bernardes R, Serranho P and Lobo C. Digital ocular fundus imaging: a review. *Ophthalmologica* 2011; 226: 161–181.
 18. Wang L, Jiang H, Grinvald A, *et al.* A mini review of clinical and research applications of the retinal function imager. *Curr Eye Res* 2018; 43: 273–288.
 19. Oishi A, Miyata M, Numa S, *et al.* Wide-field fundus autofluorescence imaging in patients with hereditary retinal degeneration: a literature review. *Int J Retina Vitreous* 2019; 5(Suppl. 1): 23.
 20. Li M, Wang H, Liu Y, *et al.* Comparison of time-domain, spectral-domain and swept-source OCT in evaluating aqueous cells in vitro. *Sci China Life Sci* 2016; 59: 1319–1323.
 21. Aumann S, Donner S, Fischer J, *et al.* Optical coherence tomography (OCT): principle and technical realization. In: Bille JF (ed.) *High resolution imaging in microscopy and ophthalmology: new frontiers in biomedical optics*. Springer, 2019. <http://www.ncbi.nlm.nih.gov/books/NBK554044/> (accessed 6 February 2022).
 22. Nahon-Estève S, Martel A, Maschi C, *et al.* Swept-source and spectral-domain OCT imaging of conjunctival tumors. *Ophthalmology* 2021; 128: 947–950.
 23. Bonin T, Franke G, Hagen-Eggert M, *et al.* In vivo Fourier-domain full-field OCT of the human retina with 15 million A-lines/s. *Opt Lett* 2010; 35: 3432.
 24. Auksorius E, Borycki D, Stremplewski P, *et al.* In vivo imaging of the human cornea with high-speed and high-resolution Fourier-domain full-field optical coherence tomography. *Biomed Opt Express* 2020; 11: 2849.
 25. Hillmann D, Pfäffle C, Spahr H, *et al.* Chapter 8: In vivo FF-SS-OCT optical imaging of physiological responses to photostimulation of human photoreceptor cells. In: Bille JF (ed.) *High resolution imaging in microscopy and ophthalmology: new frontiers in biomedical optics* [Internet]. Cham: Springer, 2019, pp. 181–194.
 26. Auksorius E. Fourier-domain full-field optical coherence tomography with real-time axial imaging. *Opt Lett* 2021; 46: 4478–4481.
 27. Pfäffle C, Spahr H, Hillmann D, *et al.* Reduction of frame rate in full-field swept-source optical coherence tomography by numerical motion correction [Invited]. *Biomed Opt Express* 2017; 8: 1499–1511.
 28. Borycki D, Hamkało M, Nowakowski M, *et al.* Spatiotemporal optical coherence (STOC) manipulation suppresses coherent cross-talk in full-field swept-source optical coherence tomography. *Biomed Opt Express* 2019; 10: 2032–2054.
 29. Valente D, Vienola KV, Zawadzki RJ, *et al.* Kilohertz retinal FF-SS-OCT and flood imaging with hardware-based adaptive optics. *Biomed Opt Express* 2020; 11: 5995–6011.
 30. Hillmann D, Spahr H, Sudkamp H, *et al.* Off-axis reference beam for full-field swept-source OCT and holoscopy. *Opt Express* 2017; 25: 27770.
 31. Dubois A, Xue W, Levecq O, *et al.* Mirau-based line-field confocal optical coherence tomography. *Opt Express* 2020; 28: 7918–7927.
 32. Suppa M, Fontaine M, Dejonckheere G, *et al.* Line-field confocal optical coherence tomography of basal cell carcinoma: a descriptive study. *J Eur Acad Dermatol Venereol* 2021; 35: 1099–1110.
 33. Verzi AE, Micali G and Lacarrubba F. Line-field confocal optical coherence tomography may enhance monitoring of superficial basal cell carcinoma treated with imiquimod 5% cream: a pilot study. *Cancers (Basel)* 2021; 13: 4913.

34. Singh M, Schill AW, Nair A, *et al.* Ultra-fast dynamic line-field optical coherence elastography. *Opt Lett* 2021; 46: 4742–4744.
35. Ruini C, Schuh S, Gust C, *et al.* Line-field optical coherence tomography: in vivo diagnosis of basal cell carcinoma subtypes compared with histopathology. *Clin Exp Dermatol* 2021; 46: 1471–1481.
36. Thomas BJ, Galor A, Nanji AA, *et al.* Ultra high-resolution anterior segment optical coherence tomography in the diagnosis and management of ocular surface squamous neoplasia. *Ocul Surf* 2014; 12: 46–58.
37. Jensen M, Israelsen NM, Maria M, *et al.* All-depth dispersion cancellation in spectral domain optical coherence tomography using numerical intensity correlations. *Sci Rep* 2018; 8: 9170.
38. Garhöfer G, Dos Santos VA, Stegmann H, *et al.* The association between tear film thickness as measured with OCT and symptoms and signs of dry eye disease: a pooled analysis of 6 clinical trials. *J Clin Med* 2020; 9: E3791.
39. Shi C, Wang M, Zhu T, *et al.* Machine learning helps improve diagnostic ability of subclinical keratoconus using Scheimpflug and OCT imaging modalities. *Eye Vis (Lond)* 2020; 7: 48.
40. Deloria AJ, Haider S, Dietrich B, *et al.* Ultra-high-resolution 3D optical coherence tomography reveals inner structures of human placenta-derived trophoblast organoids. *IEEE Trans Biomed Eng* 2021; 68: 2368–2376.
41. Gondim Teixeira PA, Villani N, Ait Idir M, *et al.* Ultra-high resolution computed tomography of joints: practical recommendations for acquisition protocol optimization. *Quant Imaging Med Surg* 2021; 11: 4287–4298.
42. Hu L, Li Y, Liu Q, *et al.* Corneal vertical and horizontal thickness profiles generated by UHR-OCT for suspected and subclinical keratoconus diagnosis. *J Refract Surg* 2021; 37: 438–445.
43. Leitgeb RA. En face optical coherence tomography: a technology review [Invited]. *Biomed Opt Express* 2019; 10: 2177.
44. Dubois A. *Handbook of full-field optical coherence microscopy: technology and applications*. CRC Press, 2016.
45. Beaurepaire E, Boccarda AC, Lebec M, *et al.* Full-field optical coherence microscopy. *Opt Lett* 1998; 23: 244–246.
46. Karamata B, Lambelet P, Laubscher M, *et al.* Spatially incoherent illumination as a mechanism for cross-talk suppression in wide-field optical coherence tomography. *Opt Lett* 2004; 29: 736.
47. Wang L, Fu R, Xu C, *et al.* Methods and applications of full-field optical coherence tomography: a review. *J Biomed Opt* 2022; 27: 050901.
48. Mazlin V, Fink M and Boccarda AC. *Full-field optical coherence tomography for non-contact cellular-level resolution in vivo human cornea imaging*. Tomographie Optique Cohérente Pour l'imagerie in Vivo de La Cornée, Université Paris sciences et lettres, 2019, <https://pastel.archives-ouvertes.fr/tel-02626956>
49. Xiao P. *Adaptive optics in full-field spatially incoherent interferometry and its retinal imaging*. PhD Thesis, Université Paris sciences et lettres, Paris, 2017.
50. Grieve K, Paques M, Dubois A, *et al.* Ocular tissue imaging using ultrahigh-resolution, full-field optical coherence tomography. *Invest Ophthalmol Vis Sci* 2004; 45: 4126–4131.
51. Assayag O, Antoine M, Sigal-Zafrani B, *et al.* Large field, high resolution full-field optical coherence tomography: a pre-clinical study of human breast tissue and cancer assessment. *Technol Cancer Res Treat* 2014; 13: 455–468.
52. Assayag O, Grieve K, Devaux B, *et al.* Imaging of non-tumorous and tumorous human brain tissues with full-field optical coherence tomography. *Neuroimage Clin* 2013; 2: 549–557.
53. Mukherjee S, Jain M, Shukla N, *et al.* Modified full-field optical coherence tomography: a novel tool for rapid histology of tissues. *J Pathol Inform* 2011; 2: 28.
54. Grieve K, Mouslim K, Assayag O, *et al.* Assessment of sentinel node biopsies with full-field optical coherence tomography. *Technol Cancer Res Treat* 2016; 15: 266–274.
55. Binding J, Ben Arous J, Leger JF, *et al.* Brain refractive index measured in vivo with high-NA defocus-corrected full-field OCT and consequences for two-photon microscopy. *Opt Express* 2011; 19: 4833–4847.
56. Tang P, Li Y, Rakymzhan A, *et al.* Measurement and visualization of stimulus-evoked tissue dynamics in mouse barrel cortex using phase-sensitive optical coherence tomography. *Biomed Opt Express* 2020; 11: 699–710.
57. Perea-Gomez A, Camus A, Moreau A, *et al.* Initiation of gastrulation in the mouse embryo is preceded by an apparent shift in the orientation

- of the anterior-posterior axis. *Current Biology* 2004; 14: 197–207.
58. Zheng JG, Lu D, Chen T, *et al.* Label-free subcellular 3D live imaging of preimplantation mouse embryos with full-field optical coherence tomography. *J Biomed Opt* 2012; 17: 070503.
 59. Zheng J, gao Huo T, Chen T, *et al.* Understanding three-dimensional spatial relationship between the mouse second polar body and first cleavage plane with full-field optical coherence tomography. *J Biomed Opt* 2012; 18: 010503.
 60. Dubois A, Grieve K, Moneron G, *et al.* Ultrahigh-resolution full-field optical coherence tomography. *Appl Opt* 2004; 43: 2874.
 61. Akiba M, Maeda N, Yumikake K, *et al.* Ultrahigh-resolution imaging of human donor cornea using full-field optical coherence tomography. *J Biomed Opt* 2007; 12: 041202.
 62. Ghouali W, Grieve K, Bellefqih S, *et al.* Full-field optical coherence tomography of human donor and pathological corneas. *Curr Eye Res* 2015; 40: 526–534.
 63. Grieve K, Thouvenin O, Sengupta A, *et al.* Appearance of the retina with full-field optical coherence tomography. *Invest Ophthalmol Vis Sci* 2016; 57: OCT96–OCT104.
 64. Bocheux R, Pernot P, Borderie V, *et al.* Quantitative measures of corneal transparency, derived from objective analysis of depth-resolved corneal images, demonstrated with full-field optical coherence tomographic microscopy. *PLoS ONE* 2019; 14: e0221707.
 65. Grieve K, Dubois A, Simonutti M, *et al.* In vivo anterior segment imaging in the rat eye with high speed white light full-field optical coherence tomography. *Opt Express* 2005; 13: 6286.
 66. Nahas A, Bauer M, Roux S, *et al.* 3D static elastography at the micrometer scale using Full Field OCT. *Biomed Opt Express* 2013; 4: 2138–2149.
 67. Apelian C, Harms F, Thouvenin O, *et al.* Dynamic full field optical coherence tomography: subcellular metabolic contrast revealed in tissues by interferometric signals temporal analysis. *Biomed Opt Express* 2016; 7: 1511.
 68. Scholler J, Groux K, Goureau O, *et al.* Dynamic full-field optical coherence tomography: 3D live-imaging of retinal organoids. *Light Sci Appl* 2020; 9: 140.
 69. Scholler J, Mazlin V, Thouvenin O, *et al.* Probing dynamic processes in the eye at multiple spatial and temporal scales with multimodal full field OCT. *Biomed Opt Express* 2019; 10: 731.
 70. Mazlin V, Xiao P, Dalimier E, *et al.* In vivo high resolution human corneal imaging using full-field optical coherence tomography. *Biomed Opt Express* 2018; 9: 557.
 71. Xiao P, Mazlin V, Grieve K, *et al.* In vivo high-resolution human retinal imaging with wavefront-correctionless full-field OCT. *Optica* 2018; 5: 409.
 72. Blavier M, Glanc M and Rousset G. Analysis of the impact of optical aberrations in en-face full-field OCT microscopy. *Opt Express* 2021; 29: 2204–2226.
 73. de Kinkelder R, Kalkman J, Faber DJ, *et al.* Heartbeat-induced axial motion artifacts in optical coherence tomography measurements of the retina. *Invest Ophthalmol Vis Sci* 2011; 52: 3908.
 74. Cai Y, Grieve K and Mecê P. Characterization and analysis of retinal axial motion at high spatiotemporal resolution and its implication for real-time correction in human retinal imaging. *Front Med (Lausanne)* 2022; 9: 868217.
 75. Xiao P, Fink M and Boccara AC. Combining FF-OCT with SD-OCT for retinal imaging. In: Boppart SA, Wojtkowski M and Oh WY (eds) *Optical coherence imaging techniques and imaging in scattering media II*. Bellingham, WA: SPIE, 2017, p. 2.
 76. Xiao P, Fink M and Boccara AC. Full-field spatially incoherent illumination interferometry: a spatial resolution almost insensitive to aberrations. *Opt Lett* 2016; 41: 3920.
 77. Barolle V, Scholler J, Mecê P, *et al.* Manifestation of aberrations in full-field optical coherence tomography. *Opt Express* 2021; 29: 220445–222206.
 78. Mazlin V, Xiao P, Scholler J, *et al.* Real-time non-contact cellular imaging and angiography of human cornea and limbus with common-path full-field/SD OCT. *Nat Commun* 2020; 11: 1868.
 79. Mecê P, Scholler J, Groux K, *et al.* High-resolution in-vivo human retinal imaging using full-field OCT with optical stabilization of axial motion. *Biomed Opt Express* 2020; 11: 492.
 80. Scholler J, Groux K, Grieve K, *et al.* Adaptive-glasses time-domain FFOCT for wide-field high-resolution retinal imaging with increased SNR. *Opt Lett* 2020; 45: 5901.
 81. Erie JC, McLaren JW and Patel SV. Confocal microscopy in ophthalmology. *Am J Ophthalmol* 2009; 148: 639–646.

82. Petropoulos IN, Ponirakis G, Khan A, *et al.* Corneal confocal microscopy: ready for prime time. *Clin Exp Optom* 2020; 103: 265–277.
83. Papanas N and Ziegler D. Corneal confocal microscopy: recent progress in the evaluation of diabetic neuropathy. *J Diabetes Investig* 2015; 6: 381–389.
84. Reilly WM and Obara CJ. Advances in confocal microscopy and selected applications. *Methods Mol Biol* 2021; 2304: 1–35.
85. Zhivov A, Stachs O, Stave J, *et al.* In vivo three-dimensional confocal laser scanning microscopy of corneal surface and epithelium. *Br J Ophthalmol* 2009; 93: 667–672.
86. Mazlin V, Irsch K, Paques M, *et al.* Curved-field optical coherence tomography: large-field imaging of human corneal cells and nerves. *Optica* 2020; 7: 872.
87. Mecê P, Groux K, Scholler J, *et al.* Coherence gate shaping for wide field high-resolution in vivo retinal imaging with full-field OCT. *Biomed Opt Express* 2020; 11: 4928.
88. Sudkamp H, Koch P, Spahr H, *et al.* In-vivo retinal imaging with off-axis full-field time-domain optical coherence tomography. *Opt Lett* 2016; 41: 4987–4990.
89. Badon A, Li D, Lerosey G, *et al.* Smart optical coherence tomography for ultra-deep imaging through highly scattering media. *Sci Adv* 2016; 2: e1600370.
90. Auksorius E and Boccara AC. High-throughput dark-field full-field optical coherence tomography. *Opt Lett* 2020; 45: 455.
91. Auksorius E and Boccara AC. Fingerprint imaging from the inside of a finger with full-field optical coherence tomography. *Biomed Opt Express* 2015; 6: 4465–4471.
92. Mazlin V, Xiao P, Irsch K, *et al.* Optical phase modulation by natural eye movements: application to time-domain FF-OCT image retrieval. *Biomed Opt Express* 2022; 13: 902.
93. Scholler J. Motion artifact removal and signal enhancement to achieve in vivo dynamic full field OCT. *Opt Express* 2019; 27: 195622–191957.
94. Hillmann D, Spahr H, Pfäffle C, *et al.* In vivo optical imaging of physiological responses to photostimulation in human photoreceptors. *Proc Natl Acad Sci USA* 2016; 113: 131383–131314.
95. Považay B, Unterhuber A, Hermann B, *et al.* Full-field time-encoded frequency-domain optical coherence tomography. *Opt Express* 2006; 14: 7661.
96. Auksorius E. Light-efficient beamsplitter for Fourier-domain full-field optical coherence tomography. *Opt Lett* 2020; 45: 1240.
97. Witmer MT and Kiss S. Wide-field imaging of the retina. *Surv Ophthalmol* 2013; 58: 143–154.
98. Lim WS, Grimaldi G, Nicholson L, *et al.* Widefield imaging with Clarus fundus camera vs slit lamp fundus examination in assessing patients referred from the National Health Service diabetic retinopathy screening programme. *Eye (Lond)* 2021; 35: 299–306.
99. Han L, Tan B, Hosseinaee Z, *et al.* Line-scanning SD-OCT for in-vivo, non-contact, volumetric, cellular resolution imaging of the human cornea and limbus. *Biomed Opt Express* 2022; 13: 4007–4020.
100. Bohn S, Sperlich K, Allgeier S, *et al.* Cellular in vivo 3D imaging of the cornea by confocal laser scanning microscopy. *Biomed Opt Express* 2018; 9: 2511–2525.
101. Ginner L, Schmoll T, Kumar A, *et al.* Holographic line field en-face OCT with digital adaptive optics in the retina in vivo. *Biomed Opt Express* 2018; 9: 472–485.
102. Liu Z, Zhang F, Zucca K, *et al.* Ultrahigh-speed multimodal adaptive optics system for microscopic structural and functional imaging of the human retina. *Biomed Opt Express* 2022; 13: 5860.